Greenland Ice Sheet wide supraglacial lake evolution and dynamics: insights from the 2018 and 2019 melt seasons

D. Dunmire[1,2], A. C. Subramanian[1], E. Hossain[3], M. O. Gani[3], A. F. Banwell[4], H. Younas[5], B. Myers[1,6]

[1]Department of Atmospheric and Oceanic Sciences, University of Colorado - Boulder, Boulder, USA
[2]Department of Earth and Environmental Sciences, KU Leuven, Belgium
[3]Department of Information Systems, University of Maryland Baltimore County, Baltimore, USA
[4]Cooperative Institute for Research in Environmental Science (CIRES), University of Colorado Boulder, Boulder, USA
[5]St. John's School, Houston, USA
[6]National Center for Atmospheric Research (NCAR), Boulder, USA

Key Points:

- We present a novel machine learning time series classification method to categorize draining, refreezing, and buried lakes on an ice-sheet-wide scale.
- We find a greater percentage of lakes drain during a warmer melt year than during a cooler one.
- Our 2-year dataset provides additional insight into dynamic factors that may control supraglacial lake hydrofracture events.

This is a non-peer reviewd pre-print. This manuscript is currently under revision at Earth and Space Sciences.

Corresponding author: Devon Dunmire, devon.dunmire@kuleuven.be

Abstract

Supraglacial lakes on the Greenland Ice Sheet (GrIS) can impact both the ice sheet surface mass balance and ice dynamics. Thus, understanding the evolution and dynamics of supraglacial lakes is important to provide improved parameterizations for ice sheet models to enable better projections of future GrIS changes. In this study, we utilize the growing inventory of optical and microwave satellite imagery to automatically determine the fate of Greenland-wide supraglacial lakes during 2018 and 2019; cool and warm melt seasons respectively. We develop a novel time series classification method to categorize lakes into four classes: 1) refreezing, 2) rapidly draining, 3) slowly draining, and 4) buried. Our findings reveal significant interannual variability between the two melt seasons, with a notable increase in the proportion of draining lakes in 2019. We also find that as mean lake depth increases, so does the percentage of lakes that drain, indicating that lake depth may influence hydrofracture potential. However, we also observe that non-draining lakes are deeper during the cooler 2018 melt season, suggesting that additional factors may predispose lakes to drain earlier in a warmer year. Our automatic classification approach and the resulting two-year ice-sheet-wide dataset provide unprecedented insights into GrIS supraglacial lake dynamics and evolution, offering a valuable resource for future research.

Plain Language Summary

Lakes form on the surface during the summer months along the margins of the Greenland Ice Sheet. Throughout the summer, these lakes can drain rapidly over a few hours or days through cracks in the ice, delivering water to the base of the ice sheet and influencing ice flow speed. At the end of the summer, remaining surface meltwater refreezes, or can sometimes remain liquid buried just beneath the surface. The varying impact that meltwater lakes can have on the ice sheet underscores the importance of understanding their seasonal evolution in different regions of the ice sheet. Here, we develop a new method to automatically categorize lakes that drain, refreeze, or become buried during a relatively cool (2018) and warm (2019) summer. We find that a higher percentage of lakes drain during a warmer year, a finding that has important implications in a warming climate. We also find that deeper lakes were more likely to drain, but that non-draining lakes were also deeper during a colder year, suggesting that other factors also contribute to lake drainage. Our new method and unique dataset provide new insight into Greenland Ice Sheet surface lake dynamics and evolution.

1 Introduction

Meltwater features on the Greenland Ice Sheet (GrIS) impact ice sheet mass balance directly by removing mass via drainage and runoff, and indirectly by influencing ice sheet dynamics (Chu, 2014). Supraglacial lakes form during the summer months along low-elevation margins of the ice sheet in persistent topological depressions driven by bed topography (Echelmeyer et al., 1991; McMillan et al., 2007; Sundal et al., 2009). Summer near-surface air temperature is non-linearly related to surface meltwater production due to the positive melt-albedo feedback (Trusel et al., 2015) and in recent years, supraglacial lakes and runoff have been observed at increasing elevations across the ice sheet (Howat et al., 2013; Leeson et al., 2015; Tedstone & Machguth, 2022), a trend that is expected to continue in a warming climate.

Supraglacial lakes can impact the ice sheet in a variety of ways. As temperatures drop below $0°C$ in the fall, remaining surface meltwater typically refreezes (Selmes et al., 2011; Johansson et al., 2013). Refrozen meltwater creates solid, impermeable ice layers, thereby increasing firn density, decreasing available firn air content, and impacting future meltwater percolation. During future melt seasons, these ice layers merge and thicken as meltwater percolates and refreezes around them, resulting in expansive ice slabs that inhibit downward percolation of meltwater (MacFerrin et al., 2019; Jullien et al., 2023) and limit future meltwater storage capacity within the firn (Machguth et al., 2016). The formation of expansive ice slabs in Greenland's accumulation zone has led to increased ice sheet runoff (MacFerrin et al., 2019; Mikkelsen et al., 2016).

In some cases however, supraglacial lakes do not refreeze entirely and meltwater can remain liquid insulated beneath the ice surface throughout the winter in features known as 'buried lakes' (Koenig et al., 2015; Law et al., 2020; Schröder et al., 2020; Dunmire et al., 2021). Buried lake meltwater storage may mitigate the ice sheet's contribution to sea level rise by storing water that might otherwise runoff (Harper et al., 2012; Forster et al., 2014); however, once meltwater fills firn pore space, this pore space cannot be regenerated quickly (Harper et al., 2012).

Supraglacial lakes can also drain throughout the melt season. These drainages can be slow, as meltwater overflows lake basins and routes through surface channels (Catania et al., 2008; Banwell et al., 2012), or rapid, as meltwater drains vertically through fractures, a process known as hydrofracture (Das et al., 2008; Tedesco et al., 2013). Hydrofracture events inject meltwater to the bed of the ice sheet which reduces basal friction and temporarily increases ice velocity (Zwally et al., 2002; Bartholomaus et al., 2008; Bartholomew et al., 2010; Hoffman et al., 2011). Moulins formed via hydrofracture can persist throughout the melt season and continually deliver meltwater to the base of the ice sheet, further affecting basal friction and ice velocity throughout the remainder of the melt season (Catania & Neumann, 2010; Banwell et al., 2016).

Given the substantial and varied impact of supraglacial lakes on the GrIS, it is important to understand when, where, and how drainage and refreezing events occur to provide improved parameterizations for ice sheet models and to better project future ice sheet changes. Previous work has detected GrIS supraglacial lakes and channels using a variety of multi-spectral satellite images including the Moderate Resolution Imaging Spectroradiometer (MODIS; Box and Ski (2007), Sundal et al. (2009), Johansson and Brown (2013), Williamson, Arnold, Banwell, and Willis (2017)), the Land Remote-Sensing Satellite System (Landsat satellites; Banwell et al. (2014), Macdonald, Banwell, and MacAyeal (2018)), Sentinel-2 (Hochreuther et al., 2021; Zhang et al., 2023), WorldView (Yang & Smith, 2013; Daneshgar et al., 2019), or a combination of these various satellites (Williamson, Banwell, et al., 2018; Wang & Sugiyama, 2024). More recently, Sentinel-1 Synthetic Aperture Radar (SAR) observations have been used to detect supraglacial and buried meltwater features across the GrIS (Miles et al., 2017; Schröder et al., 2020; Dunmire et al., 2021; Benedek & Willis, 2021; Zheng et al., 2023). SAR can be used year round, regardless of the weather, and can penetrate the surface and detect meltwater buried several meters beneath the surface (Rignot et al., 2001).

Current work investigating the seasonal evolution of GrIS supraglacial lakes is mostly limited to a regional or individual drainage basin scale (McMillan et al., 2007; Sundal et al., 2009; Morriss et al., 2013; Turton et al., 2021; Otto et al., 2022; Wang & Sugiyama, 2024; Glen et al., 2024), or is more than a decade old and relies on low-resolution MODIS imagery for lake tracking (Selmes et al., 2011, 2013). Here, we develop and present a novel classification method that utilizes time series of features from both optical and microwave imagery to automatically classify GrIS supraglacial lakes into four behavioral categories: 1) refreezing, 2) rapidly draining, 3) slowly draining, and 4) those that transition to buried lakes by the end of the melt season. We apply our classification method to supraglacial lakes previously identified during the 2018 and 2019 melt seasons (Dunmire et al., 2021), a cold and warm year respectively. In doing so, we provide a comprehensive dataset of ice-sheet-wide lake drainage events and new insight into lake drainage and refreeze that will aide future GrIS supraglacial lake and hydrofracture research.

2 Data

2.1 Greenland supraglacial lake dataset

For this study, we used the pan-Greenland supraglacial lake dataset from Dunmire et al. (2021). This dataset contains high-resolution (30 m) outlines for supraglacial lakes with a surface area > 0.05 km^2 from the 2018 and 2019 melt seasons across the 6 major GrIS drainage basins, defined by Rignot and Mouginot (2012) (SW, CW, NW, NO, NE, and SE). The dataset additionally provides lake surface area information and the elevation for each supraglacial lake from the Greenland Ice Mapping Project (GIMP) elevation dataset (Howat et al., 2015). There are 3846 supraglacial lakes in 2018 and 6146 in 2019 (Dunmire et al., 2021). We chose this dataset because it covers the entire ice sheet and is available at a high spatial resolution.

2.2 Satellite imagery

We obtained imagery from three different satellites on the Google Earth Engine (GEE) platform (Gorelick et al., 2017): Sentinel-1 (S1, microwave), Sentinel-2 (S2, optical), and Lansdat 8 (L8, optical). We utilized available imagery from these satellites between January 1, 2018 and December 31, 2019.

The S1 satellite provides C-band SAR backscatter imagery over the entire GrIS. For 2018 and 2019, the dual S1A and S1B satellites provided a maximum 6-day repeat observation cycle. We used the horizontally-transmitted, vertically-received (HV) band of the Interferometric Wide swath mode, which is available at a 10 m horizontal resolution.

For optical imagery, we used the S2 Level-1C orthorectified top-of-atmosphere reflectance. Of the 13 spectral bands available from the S2 data, we used Band 2 (Blue, 20 m horizontal resolution), Band 3 (Green, 20 m), Band 4 (Red, 20 m), Band 10 (Cirrus, 60 m) and Band 11 (SWIR 1, 20 m). We also obtained optical imagery from the Landsat 8 calibrated top-of-atmosphere reflectance collection, utilizing Band 2 (Blue, 30 m), Band 3 (Green, 30 m), Band 4 (Red, 30 m), and Band 6 (SWIR 1, 30 m).

2.3 Regional Climate Modeling data

We obtained near-surface (2 m) air temperature data from the west-domain of the Copernicus Arctic Regional Reanalysis product (CARRA-West; Schyberg et al. (2020)). This product provides 3-hourly analyses at a 2.5 km spatial resolution over the GrIS and is forced at the boundaries with ERA5 for the period of 1991 – present. For each supraglacial lake outline in 2018 and 2019, we obtained an annual time series of mean daily near-surface air temperatures from the CARRA-West grid cell containing the lake.

3 Methodology

3.1 Satellite Imagery Preprocessing

3.1.1 S1 imagery time series

S1 imagery available on GEE is already preprocessed with the following steps: (1) thermal noise removal, (2) radiometric calibration, (3) terrain correction using ASTER DEM, and (4) values converted to decibels via log scaling. For each 2018 and 2019 supraglacial lake outline (Dunmire et al., 2021), we utilized all available S1 imagery from January 1 through December 31 of the year the lake was detected. Then, from every available S1 image, we computed the average HV value within each lake outline (HV_{lake}) and the average HV value within 750 m outside the lake bounds ($HV_{background}$). We then computed a backscatter anomaly for the lake (HV_{anom}) following Equation 1:

$$HV_{anom} = HV_{lake} - HV_{background} \quad (1)$$

By computing a backscatter lake anomaly, we can better compare imagery between orbits with different incidence angles. To obtain a complete annual time series of HV_{anom} for each lake, we linearly interpolated between all observations. We then further smoothed variability between observations from different S1 orbits by applying a 12-day smoothing filter. (e.g. Fig. S1).

3.1.2 Optical imagery time series

S2 images with $\leq$ 90% cloud coverage were obtained for each lake between May 1 and October 15 during the year that the lake was detected. Because top-of-atmosphere S2 imagery in GEE is scaled by a factor of 10,000, we first divided all spectral bands by 10,000. For each image we then created a cloud pixel mask and a water pixel mask. Clouds in S2 imagery were masked following Moussavi et al. (2020) where SWIR (B11) $>$ 0.1 or Cirrus (B10) $>$ 0.1. Water was masked where the Normalized Difference Water Index (NDWI, Equation 2) $>$ 0.18 (Moussavi et al., 2016; Pope et al., 2016; Yang & Smith, 2013; Moussavi et al., 2020). We did not use the Green - Red $>$ 0.09 threshold for masking water from Moussavi et al. (2020) because we found that this excluded parts of lakes with deep water.

We performed a similar cloud and water masking procedure for L8 imagery. Following Moussavi et al. (2020), we masked pixels as clouds where the Normalized Difference Snow Index (NDSI, Equation 3) $<$ 0.8 or where SWIR (B6) $>$ 0.1. Water in L8 images was masked where NDWI $>$ 0.19 and where Blue - Green $>$ 0.7. Again, we did not use the Green - Red $>$ 0.7 from Moussavi et al. (2020) because this threshold excluded deeper water.

$$NDWI = \frac{Blue - Red}{Blue + Red} \quad (2)$$

$$NDSI = \frac{Green - SWIR}{Green + SWIR} \quad (3)$$

For both S2 and L8 imagery, we did not compute a Rock/Seawater mask because we had pre-defined supraglacial lake outlines from Dunmire et al. (2021). After creating the cloud and water pixel masks for all S2 and L8 image, for each lake we then removed images with pixels inside the lake's bounds masked as clouds. We then computed the percentage of pixels within the lake bounds masked as water (p_{water}). We determined p_{water} for each lake individually and from every non-cloudy optical image. We also obtained the average solar zenith angle (SZA) within each of the lake bounds from every optical image.

After combining p_{water} from S2 and L8 imagery for a lake, the following steps were taken at each time step t to remove outlier observations:

1. The observation was removed if:
   - $p_{water}(t) > 0.05$, and
   - $SZA(t) > 75°$

   This was often the case during shoulder seasons when shadows were misclassified as water (e.g. Fig. S2a).
2. The observation was removed if:
   - $p_{water}(t) > 0.4$, and
   - $p_{water}(t-1) < \frac{1}{2} p_{water}(t)$, and

- $p_{water}(t+1) < \frac{1}{2}p_{water}(t)$, and
- at a previous time step ($t_{prev.}$): $p_{water}(t_{prev.}) > 0.8$

This was often the case if there were cloud shadows within the lake bounds or for shadows not removed in Step 1 (e.g. Fig. S2b). The specification that the lake previously had to have water ($p_{water}(t_{prev.}) > 0.8$) was applied so that observations where the lake filled and drained rapidly were not excluded.

3. The observation was removed if:
   - $p_{water}(t-1) - p_{water}(t) > 0.2$, and
   - $p_{water}(t+1) - p_{water}(t) > 0.2$

   These outliers existed if clouds were missed by the cloud mask (e.g. Fig. S2c).

Finally, we linearly interpolated all observations to obtain an annually complete time series of p_{water} for each lake.

3.2 Supraglacial lake classification

3.2.1 Supraglacial lake classes

Here, we classify supraglacial lakes into four categories based on their evolution throughout the melt season. These lake classes are: 0) refreezes, 1) rapidly drains, 2) slowly drains, and 3) becomes buried (Fig. 1). To create the training dataset for our model, which automatically classifies supraglacial lakes into these four classes, we manually labeled 1000 lakes, with 250 for each class. We defined rapidly draining lakes to be where p_{water} decreases to 20% of the lake's maximum value in a period shorter than 6 days, following Morriss et al. (2013). While rapid drainage events can be defined over periods shorter than this (i.e 2 days: (Das et al., 2008; Tedesco et al., 2013; Selmes et al., 2011) or 4 days: (Williamson, Willis, et al., 2018; Doyle et al., 2014)), we use a more relaxed threshold to accommodate the sometimes limited temporal resolution of clear-sky optical imagery (Morriss et al., 2013).

Supraglacial lakes were labeled from all 6 GrIS regions and confirmed using GEE optical and microwave imagery. Figure 1 shows example time series of p_{water} and HV_{anom} for a lake from each class. From our labeled lakes dataset, we used 80% for training our model, and set aside the remaining 20% for final model testing.

3.2.2 Time series classification model selection

Various deep learning techniques have been proposed for time series classification including recurrent neural network-based models, distance-based models, feature-based models, interval-based models, and kernel-based models. To classify supraglacial lakes using the p_{water} and HV_{anom} time series, we utilized the *sktime* Python time series classification package (Löning et al., 2019). From *sktime*, we explored the recurrent neural network-based algorithm LSTMFCNClassifier (Karim et al., 2019), distance-based algorithm KNeighborsTimeSeriesClassifier, feature-based algorithm RandomIntervalClassifier, kernel-based algorithm RocketClassifier (Dempster et al., 2020), and three interval-based algorithms CanonicalIntervalForest (Middlehurst et al., 2020), SupervisedTimeSeriesForest (Cabello et al., 2020), TimeSeriesForestClassifier (Deng et al., 2013).

Before training the models, we normalized the timeseries data into the range of [0,1]. The aforementioned models are evaluated with two different feature sets: one with only HV_{anom}, and one with both HV_{anom} and p_{water}, to determine the added benefit of including time series from optical imagery, which typically has more limited temporal coverage than microwave imagery. We did not train a model with only p_{water} because the optical imagery alone is insufficient to identify buried lakes. To avoid overfitting, we applied a k-fold cross-validation with 5 folds, where the model is alternatively tested on

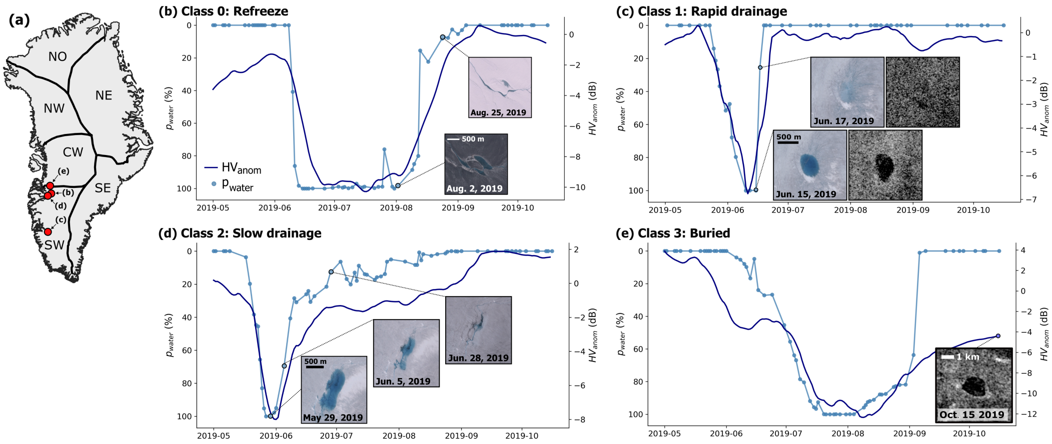

Figure 1. Example optical and microwave time series for each supraglacial lake class. (a) Map of GrIS with lakes in b-e indicated with red dots, (b) refreeze (class 0), (c) rapidly drains (class 1), (d) slowly drains (class 2), and (e) becomes buried (class 3). Light blue lines indicate p_{water}, with dots for each optical image of the lake (left y-axis) and dark blue lines represent time series of HV_{anom} (left y-axis).

one fold and trained on the other 4 folds. We trained the models using the previously mentioned 1000 manually labeled supraglacial lakes, with 250 for each class (refreeze, rapid drain, slow drain, and buried).

Table S1 summarizes the resulting accuracy from this cross-validation for the different time series classification techniques. We observe that the performance of all models improved substantially when p_{water} is incorporated, which is understandable given that p_{water} provides additional useful information for the lake classifications. Moreover, out of the 7 classification techniques, RocketClassifier achieved the most consistently high accuracy in all scenarios (with and without p_{water} and using cross-validation). In addition, RocketClassifier has a significant computational advantage over the other complex architectures of the other models. Therefore, we used RocketClassifer for the remainder of this study.

3.2.3 Time series classification with ROCKET

RocketClassifier (ROCKET, RandOM Convolutional KErnal Transform; Dempster et al. (2020)) has previously been evaluated on benchmark datasets in the UCR Archive (Dau et al., 2018) and can achieve the same accuracy as competing state-of-the-art algorithms in a fraction of the training time. ROCKET applies random convolutional kernels to transform the time series into features and then uses a linear classifier trained with the features. We used 10,000 convolutional kernels and the linear Ridge Classifier from the *scikit learn* python package (Pedregosa et al., 2011). We trained two separate ROCKET models: one that classifies lakes using the optical p_{water} lake time series ($ROCKET_{op}$) and one that classifies lakes using the microwave HV_{anom} lake time series ($ROCKET_{mic}$). Using these two separate models allows us to classify lakes using one imagery source if the other is inadequate (i.e. limited availability of cloud-free optical images for a lake, Fig. S3b). Because buried lakes are invisible in optical imagery, $ROCKET_{op}$ will never be able to classify buried lakes correctly. As such, $ROCKET_{op}$ was only trained to classify lakes into classes 0, 1 and 2.

3.2.4 End-model to resolve classification discrepancies

In some cases, the time series created from microwave and optical imagery do not agree, resulting in different lake classifications from the $ROCKET_{op}$ and $ROCKET_{mic}$ models (Fig. S3). To resolve discrepancies between $ROCKET_{op}$ and $ROCKET_{mic}$ classifications, we further trained an end-model that uses the following features to make a final classification for the lake:

- $ROCKET_{op}$ prediction (categorical)
- $ROCKET_{op}$ class 0 (refreeze) confidence score(numerical)
- $ROCKET_{op}$ class 1 (rapid drain) confidence score(numerical)
- $ROCKET_{op}$ class 2 (slow drain) confidence score(numerical)
- $ROCKET_{mic}$ prediction (categorical)
- $ROCKET_{mic}$ class 0 (refreeze) confidence score(numerical)
- $ROCKET_{mic}$ class 1 (rapid drain) confidence score(numerical)
- $ROCKET_{mic}$ class 2 (slow drain) confidence score(numerical)
- $ROCKET_{mic}$ class 3 (buried) confidence score (numerical)
- lake elevation (numerical)
- lake area (numerical)
- maximum p_{water} during the season (numerical)
- number of days it takes for p_{water} to decrease to 20% of the lake's maximum value ('drain time', numerical)
- temporal resolution of S1 observations during drain time (numerical)
- temporal resolution of optical observations during drain time (numerical)
- Average HV_{anom} for the lake between October 15 and November 1 (numerical)

The confidence score for each class comes from the sklearn RidgeClassifier model output and is proportional to the signed distance of that sample to the hyperplane. We trained the end-model using the *PyCaret* python package for automating machine learning workflows (Moez, 2020). Numerical features were normalized and categorical features were one-hot encoded. We used 5-fold cross-validation to compare PyCaret classification models and to tune our model with a grid search of 500 iterations. With a cross-validation F1 score of 0.9543, the optimal end-model was a CatBoost classifier (Prokhorenkova et al., 2018).

This end-model was only applied when discrepancies between $ROCKET_{op}$ and $ROCKET_{mic}$ exist. Examples of such discrepancies are for buried lakes (because $ROCKET_{op}$ will never be able to classify buried lakes, e.g., Fig. S3b), lakes at low elevation where the HV_{anom} time series is similar to that of buried lakes (e.g., Fig. S3c), or lake drainage events where the HV_{anom} time series does not capture the drainage in the same way as the p_{water} time series (e.g., Fig. S3d). If, for a given lake, the classifications from $ROCKET_{op}$ and $ROCKET_{mic}$ were the same, then this classification was the final label given to the lake, and the end-model was not utilized.

After training $ROCKET_{op}$, $ROCKET_{mic}$, and the end-model, we tested our entire pipeline on 200 independent samples ($\sim$50 per class). On this test sample, our model had 98% accuracy and an F1 score of 0.98, with confusion for 4 lakes between the refreeze and slow drain classes (Fig. S4).

3.3 Supraglacial lake analysis

After training and testing our approach, we applied our model on all 2018 and 2019 supraglacial lakes, giving each lake a label based on its evolution throughout each melt season.

3.3.1 Lake depth

For each lake with a maximum $p_{water} > 0.5$ and no greater than a 31 day gap between optical observations, we calculated the mean lake depth at the time when p_{water} was at its maximum. First, we found the date of maximum p_{water} for the lake. Then, using GEE, we retrieved either the S2 or L8 image from this date, preferring to use S2 where possible due to S2's higher spatial resolution. To compute lake depth for each pixel (z_{pix}), we followed Williamson, Banwell, et al. (2018), which uses Equation 4 below, developed by Pope et al. (2016) based on the attenuation of optical light in a water column:

$$z_{pix} = \frac{[ln(A_d - R_\infty) - ln(R_{pix} - R_\infty)]}{g}, \quad (4)$$

where A_d is the lake-bottom albedo, R_∞ is the reflectance for optically deep water, and R_{pix} is the pixel reflectance, and g is the coefficient for the losses in upward and downward travel through a water column. For both S2 and L8 imagery, we averaged depths calculated using the red (B4) and green (B3) top-of-atmosphere reflectance data. A_d was calculated as the average reflectance of the relevant band for the ring of pixels immediately surrounding the lake (ring of 3 pixels for S2; Williamson, Banwell, et al. (2018)) and R_∞ was approximated as 0 (Banwell et al., 2019; Dell et al., 2020). For L8 imagery, we used $g = 0.7507$ for the red band and $g = 0.1413$ for the green band (Pope et al., 2016). We used S2 g values determined by Williamson, Banwell, et al. (2018) ($g = 0.8304$ for the red band and $g = 0.1413$ for the green band). We determined the mean lake depth after calculating z_{pix} for each pixel within the lake bounds.

3.3.2 Drainage date

For each supraglacial lake that was labeled to have undergone rapid drainage, we also determined the drainage date. To do this, we found the last time step t where $p_{water}(t) < 0.8$ and $p_{water}(t) < max(p_{water})$. Even though this time step is before the respective lake drainage event, we label it as the 'drainage date' as it is the last available optical image where the lake is full of water.

4 Results

Comparing our results for the colder 2018 and warmer 2019 melt seasons, we observe both interannual variability in surface meltwater production and total number of supraglacial lakes, as well as a shift in supraglacial lake dynamics (Fig. 2, Tab. S2). The total number of supraglacial lakes increases by 60% from 2018 (3846 lakes) to 2019 (6146 lakes) (Dunmire et al., 2021). Correspondingly, there is a substantial expansion in supraglacial lake area, increasing from 1242 km^2 in 2018 to 2569 km^2 in 2019 (+107%). Despite a more than doubling of supraglacial lake area between the two years, in this study we find that refrozen lake area increases by only 7.6% and the total number of refreezing lakes actually decreases from 1330 lakes (34% of all 2018 lakes) to 1096 lakes (18% of all 2019 lakes). The proportion of refreezing supraglacial lakes changes the most drastically in the Northern GrIS regions. For example, in NO Greenland, more than 50% of identified supraglacial lakes refreeze in 2018 while only 21% refreeze in 2019, with the total refrozen lake area actually diminishing by 27%.

Coincident with the observed decrease in the proportion of refreezing lakes in 2019, we observe a substantial rise in the proportion of lakes that drain slowly, increasing from 26% of all GrIS supraglacial lakes in 2018 to 40% in 2019. Again, this change is most prominent in the Northern GrIS regions, where the incidence of slowly draining lakes increases by 190%, 269%, and 334% in the NW, NO, and NE, respectively.

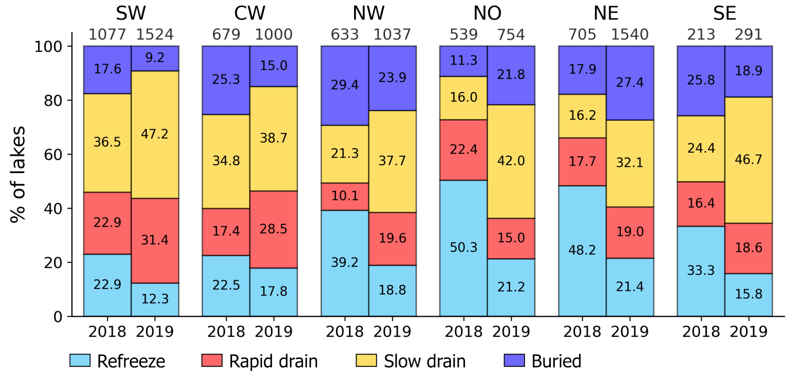

Figure 2. The percentage of lakes that refreeze, drain rapidly, drain slowly, or become buried in 2018 and 2019 for each GrIS region (as indicated in Fig. 1.)

Figure 3 illustrates this shift from predominately refreezing lakes in 2018 to draining lakes in 2019 for a case study area in NE Greenland. Within this approximately 20 x 15 km^2 region, 16 distinct lakes were detected in 2018 (Fig. 3b,c) and 15 were detected in 2019 (Fig. 3d,e). The onset of mean daily air temperatures above freezing for this region in 2019 occurs on June 11 (Fig. 3h). Over the ensuing week (June 11 - June 17), the mean 2019 air temperature is 6.7 $°C$ higher compared to the corresponding period in 2018, during which the mean daily air temperature remains below freezing until June 25. During July and August, mean air temperatures remain 2.7 $°C$ cooler in 2018 relative to 2019.

We suggest that this interannual variability in air temperature not only results in differences in surface meltwater production between the two melt seasons, but also a shift in supraglacial lake dynamics. For example, in this area of NE Greenland, 11 of 16 (69%) lakes refreeze during the 2018 melt season (Fig. 3f). In contrast, in 2019 (Fig. 3g), nearly all the lakes drain either slowly (9 of 15, 60%) or rapidly (4 of 15, 27%). Despite late August 2018 experiencing average air temperatures nearly 4 $°C$ cooler than the same period in 2019, we observe a greater presence of ponded meltwater during this period in the 2018 melt season (Fig. 3c,e). The absence of ponded meltwater in late August 2019 is attributed to the lakes in this area having previously drained.

The proportion of lakes that rapidly drain also increases between the two years, from 18% of all GrIS lakes in 2018 to 23% in 2019. The relative increase in rapid lake drainage events is most substantial in Western Greenland, where the number of rapid lake drainages increases by 93%, 141%, and 217% in the SW, CW, and NW regions respectively, despite these regions experiencing 41%, 47%, and 64% increases in the total number of supraglacial lakes. Figure 4 demonstrates this shift for a case study area in CW Greenland. Within this area, 4 of the 18 (22%) identified supraglacial lakes refreeze in 2018, with the remaining lakes transitioning to buried lakes at the end of the melt season (4b, e). There are no lake drainage events in this area in 2018. In contrast, in 2019, 9 of the 17 (53%) identified lakes drain rapidly, with a multi-lake hydrofracture event occurring sometime between July 23 and 26, 2019 (4c,d,f). In this area, early season (May 1 - June 15) average daily air temperatures are substantially warmer (+5.9 $°C$) in 2019 relative to 2018. Despite the daily mean air temperature rising above freezing for the first time earlier during the 2018 melt season (June 4), throughout the remainder of June and July 2019, daily air temperatures remain 2.1 $°C$ warmer than in 2018. Much of this area in the CW region is located relatively far inland, and the 2019 rapidly draining lakes here have an average elevation of 1490 m, higher than the 99th percentile elevation for rapidly draining lakes in CW Greenland in 2018.

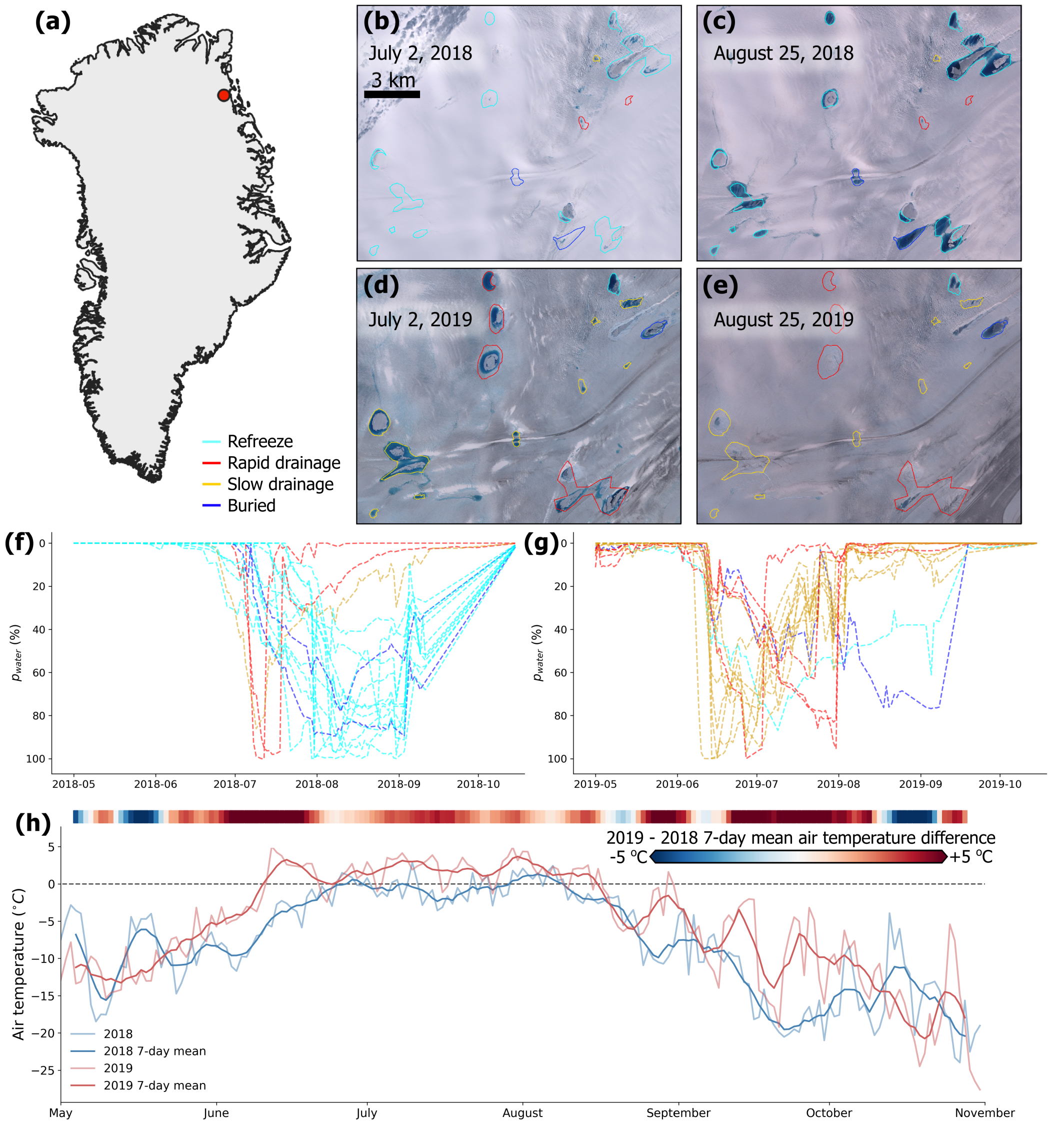

Figure 3. Example supraglacial lake changes for a case study area in NE Greenland, indicated by the red dot in (a). (b-e) S2 imagery from July 2, 2018 (b), August 25, 2018 (c), July 2, 2019 (d) and August 25, 2019 (e). 2018 (b,c) and 2019 (d,e) Detected lakes from 2018 (b,c) and 2019 (d,e) are outlined and colored corresponding to their evolution classification throughout the melt season. (f-g) Time series of p_{water} for each lake in 2018 (f) and 2019 (g). Time series are colored corresponding to the each lake's evolution classification. (h) Time series of mean daily air temperature for this region in 2018 (blue) and 2019 (red). The colored bar at the top of the plot represents the difference in 7-day mean air temperatures between the two years (2019 - 2018).

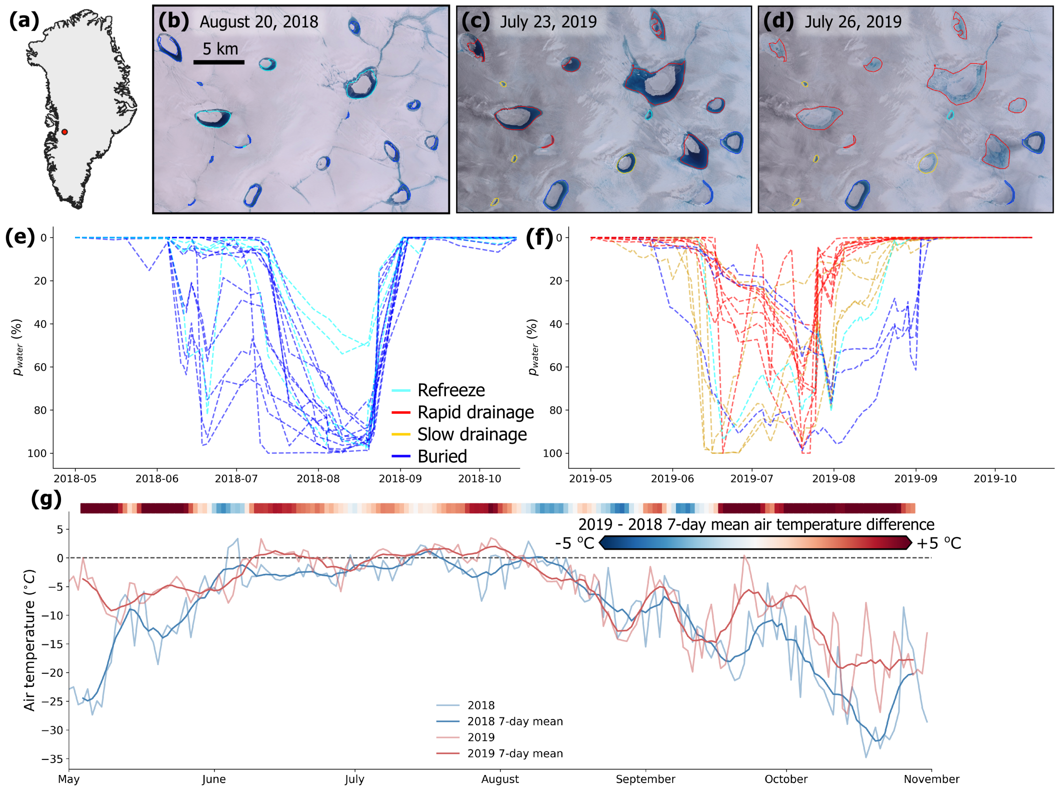

Figure 4. Example supraglacial lake changes for a region in CW Greenland (a). (b-d) S2 imagery from August 20, 2018 (b), July 23, 2019 (c), and July 26, 2019. Detected lakes from 2018 (b) and 2019 (c,d) are outlined and colored corresponding to their evolution classification throughout the melt season. (f-g) Time series of p_{water} for each lake in 2018 (e) and 2019 (f). Time series are colored corresponding to the lake's evolution classification. (g) Time series of mean daily air temperature for this region in 2018 (blue) and 2019 (red). The colored bar at the top of the plot represents the difference in 7-day mean air temperatures between the two years (2019 - 2018).

In accordance with Selmes et al. (Selmes et al., 2013), we observe, across all regions of the GrIS and over both years, that draining lakes are located at lower elevations than lakes that refreeze or become buried (Fig. 5). In the Northern GrIS regions (NW, NO, and NE), where lakes typically form at lower elevations, rapid lake drainages occur at a mean elevation of 641 ± 361 m (± 1 standard deviation) and slow lake drainages occur at a mean elevation of 752 ± 346 m. In contrast, lakes that do not drain, but either refreeze or become buried, are located at mean elevations of 939 ± 381 m and 1099 ± 390 m, respectively. In Southern Greenland (SW, CW, SE), rapid and slow drainage events occur at mean elevations of 1159 ± 323 m and 1199 ± 298 m, respectively, while refreezing and buried lakes are located at average elevations of 1408 ± 267 m and 1544 ± 227 m.

Figure 5 also demonstrates that draining lakes are typically deeper than non-draining lakes. During both years, the mean depth for all rapidly draining lakes is 3.27 ± 0.99 m and varies about 35% between the six regions, with a minimum mean depth of 2.81 m in NO Greenland and a maximum mean depth of 3.62 m in SE Greenland. The regional variability in mean lake depth for other types of lakes is slightly larger, from 1.80 m (NO) to 2.99 m (SE) for refreezing lakes (47% of the mean), 2.06 m (NO) to 3.32 m (SE) for slowly draining lakes (43% of the mean), and 1.78 m (NO) to 3.12 m (SE) for buried lakes (54% of the mean).

Across the entire ice sheet, and for both years, 56% of lakes drain either rapidly or slowly. However, for lakes with a mean depth < 2 m, only 35% drain, with proportionally more refreezing or becoming buried (36% refreeze, 29% buried). In addition, most lakes that drain with mean depths shallower than 2 m drain slowly (27%), as opposed to rapidly (8%). As lakes deepen, there appears to be an increasing likelihood that they will drain, particularly rapidly, and a decreasing likelihood of refreezing (Fig. 6). For example, above 4 m depth, 70% of lakes drain (35% rapidly and 35% slowly).

Surprisingly, we find that lakes are deeper on average during the colder 2018 melt season (Fig. 7). The ice-sheet-wide mean lake depth in 2018 is 3.06 m, compared to 2.66 m in 2019, an approximate 13% reduction in mean lake depth. The depth reduction from 2018 to 2019 is greatest in NO Greenland, where the 2018 mean depth (2.36 m) is 21% deeper than in 2019 (1.87 m), and smallest in SW Greenland, where the 2018 mean depth (3.00 m) is only 3% deeper than in 2019 (2.91 m). The mean lake depth difference between 2018 and 2019 is also substantially larger for lakes that do not drain rapidly (Fig. 7). For example, refreezing lakes have a mean depth of 2.87 m in 2018 and 2.11 m in 2019, a 26% reduction. The reduction in mean depth from 2018 to 2019 is only 2.7% for rapidly draining lakes.

Finally, we observe that rapid lake drainages occur earlier during the 2019 melt season compared to 2018. The mean drainage date across all regions during the 2019 melt season (June 22 ± 20 days) is 17 days earlier than in 2018 (July 9 ± 15 days); a difference that is fairly consistent across all 6 regions. Figure 8 demonstrates a major change in the timing of lake drainage for a case study area in NE Greenland. In 2019, lakes in the area delineated by the black box in Figure 8 drain between June 13 and 18, an average of 44 days earlier than in 2018. This 2019 drainage period is also even before meltwater begins to pond on the surface during the 2018 melt season. In 2018, lakes in this area form after July 1 and drain primarily between July 28 and August 1. Also notable is that these lakes in 2018 have a larger surface area compared to 2019 (mean of 0.48 km^2 in 2018 compared to 0.28 km^2 in 2019) and remain full for a longer period of time before draining (Fig. 8c).

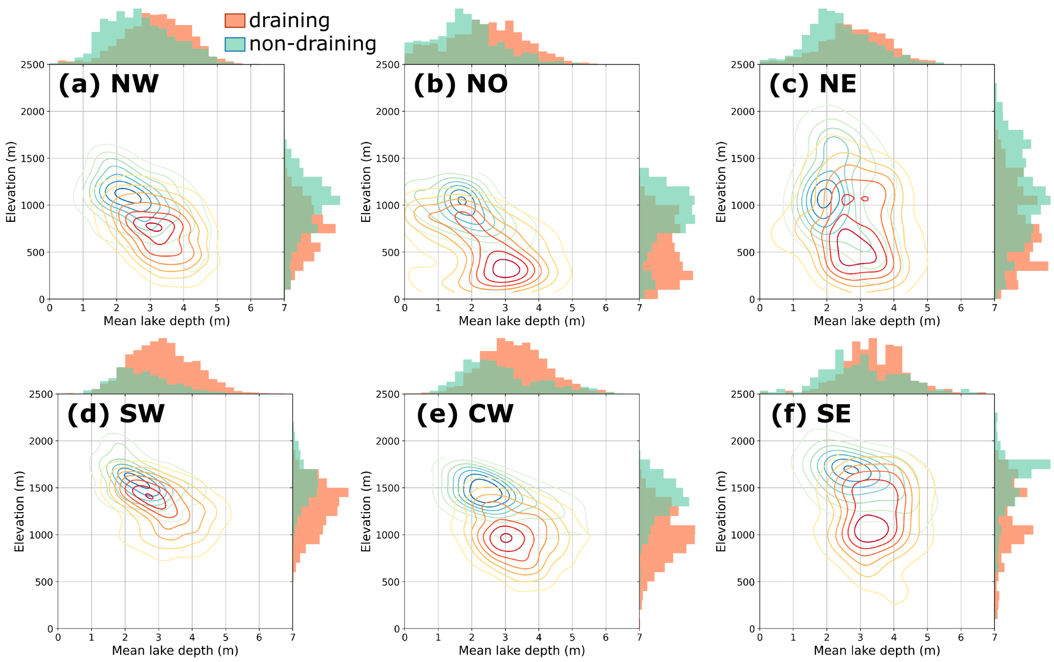

Figure 5. 2D histograms of mean lake depth vs. elevation for each region of the GrIS (includes both 2018 and 2019 lakes). The distribution for lakes that drain (either rapidly or slowly) is shown in red-orange while the distribution for lakes that do not drain (refreezing or buried lakes) is shown in blue-green.

5 Discussion

After applying our novel time series classification model, utilizing time series of both optical and microwave imagery, to a dataset of supraglacial lakes across the entire GrIS, we find that 18% and 23% of all lakes drain rapidly in 2018 and 2019, respectively. These proportions are larger than the 13% reported by Selmes et al. (2011), in which 2600 lakes were mapped over 5 different years (2005–2009). While this present study only spans 2 years, it includes nearly 10000 lakes and incorporates lakes smaller than those studied in Selmes et al. (2011), which was made possible by the finer spatial resolution available from the S1 and S2 imagery.

Additionally, previous work has concluded that interannual variability in lake evolution is much smaller than regional variability (Selmes et al., 2011, 2013). The work presented here does not support this conclusion. For example, in 2018 the percentage of refreezing lakes varies regionally from 22.5% in CW Greenland to 50.3% in NO Greenland, comparable to the interannual change in the percentage of refreezing lakes in NO Greenland between 2018 and 2019 (51.3% and 21.2%, respectively). This finding suggests that climatic controls, particularly near surface air temperature, effect not only the amount of surface meltwater production, but also how hydrologic systems develop and evolve throughout the melt season.

During the warmer 2019 melt season there were more supraglacial lakes and therefore more supraglacial lake drainage events. Importantly, however, in this study we also observe an increased proportion of draining lakes in 2019 relative to 2018 (Fig. 2). These findings have important implications in a warming climate. During future warmer melt seasons we can expect (a) increased runoff which enhances surface mass loss (Trusel et al., 2018; Hanna et al., 2008), (b) increased total volume of meltwater injected to the bedrock

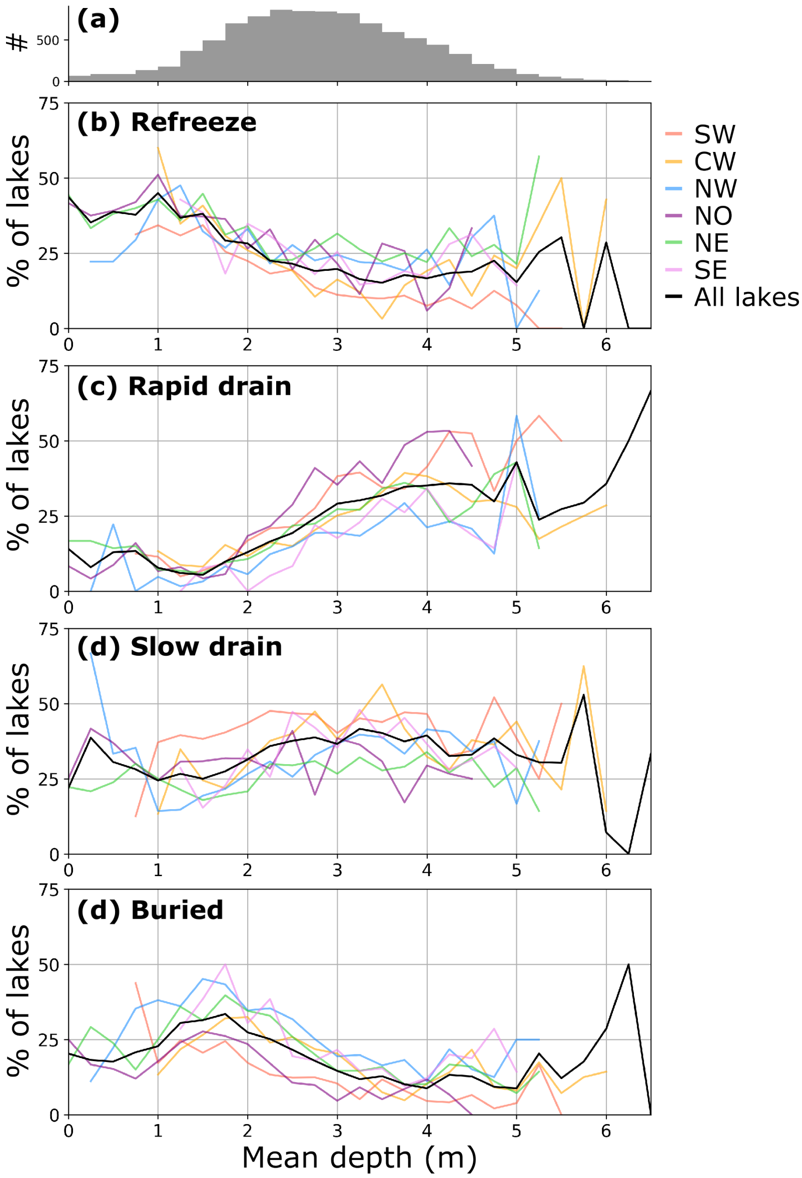

Figure 6. Percentage of lakes classified into each class with mean lake depth. (a) Histogram distribution of mean lake depths, including both 2018 and 2019 lakes. (b-d) The percentage of all lakes that refreeze (a), drain rapidly (b), drain slowly (c), or become buried (d) with increasing mean lake depth. Data is only plotted for each region if there are 5 or more lakes with that mean depth.

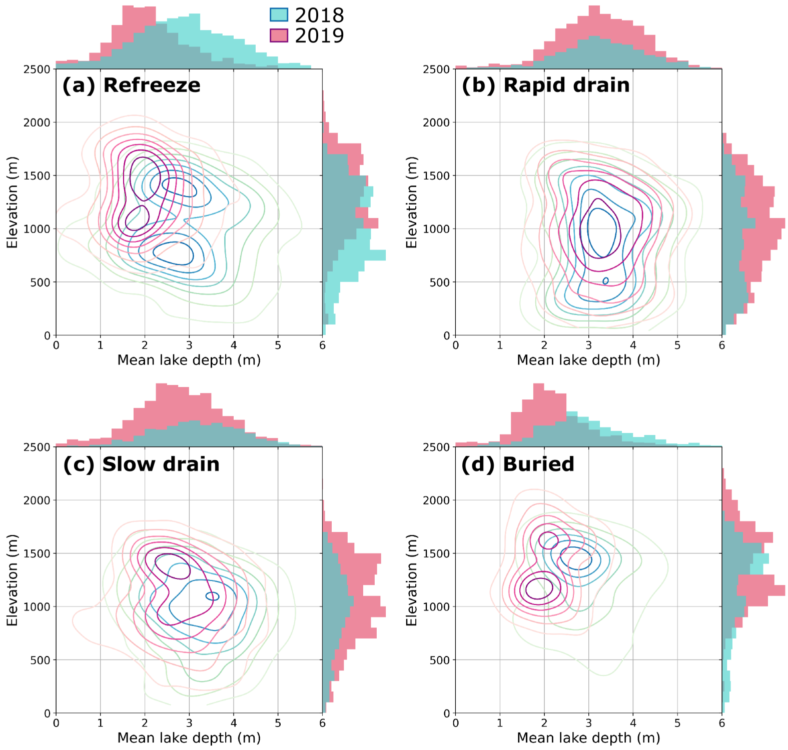

Figure 7. 2D histograms of maximum lake depth vs. elevation for each type of lake, compared between years. The distribution for 2018 lakes is shown in blue-green while the distribution for 2019 lakes is shown in pink-red.

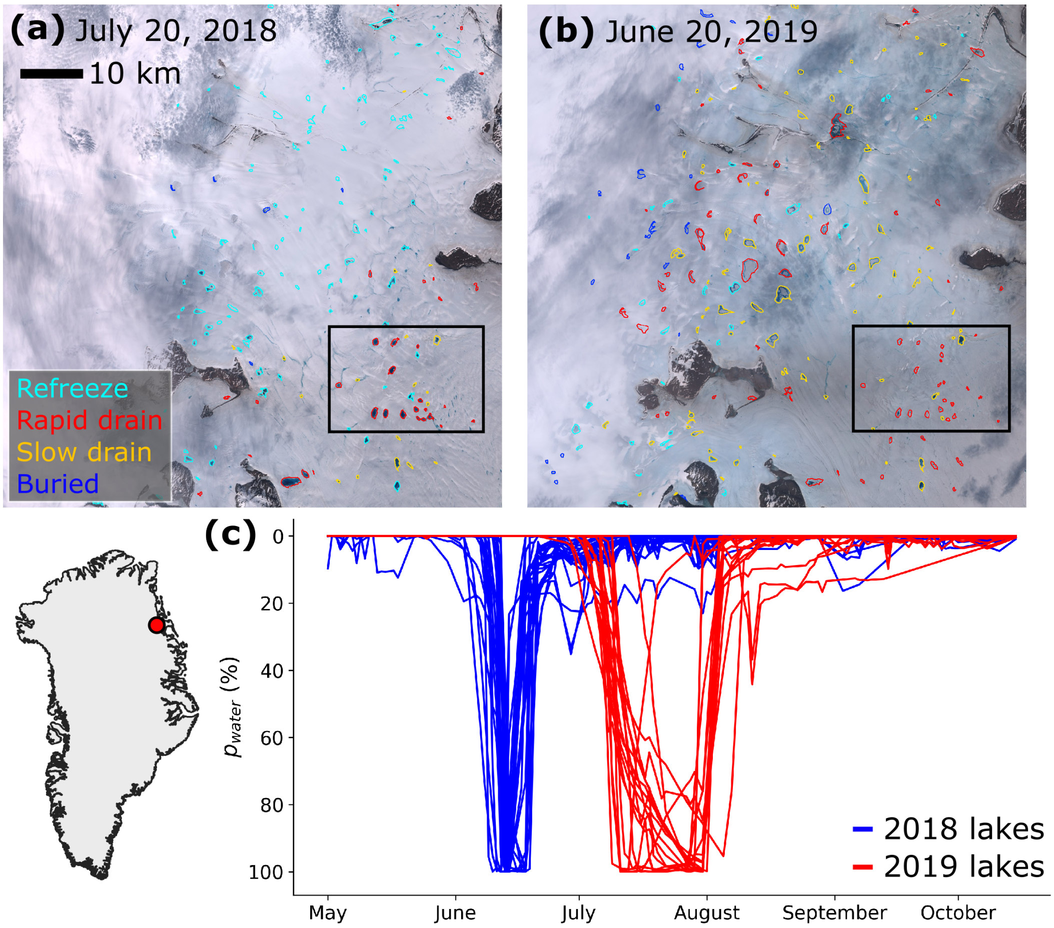

Figure 8. Interannual supraglacial lakes drainage date comparison in NE Greenland. (a) S2 image from July 20, 2018, with lakes outlined according to their classification. S2 image from June 20, 2019 with lakes outlined according to their classification. (c) Time series of p_water for rapidly draining lakes for a area outlined by the black box in (a) and (b).

and (c) increased moulin density as a result of more rapid lake drainages, which in turn impacts subglacial water pressures, basal sliding rates, and ice motion (Banwell et al., 2016). Given the proportional increase in both slow and rapid lake drainages and proportional decrease in refreezing lakes between 2018 and 2019, we hypothesize that these processes may act non-linearly in a warming climate.

Our new method enables large-scale, ice-sheet-wide classification of draining and refreezing lakes, providing us with a comprehensive dataset of lake drainage events, and new insights into the potential controls on lake drainage. Previous work has suggested that an upper elevation hydrofracture limit ($\sim$1600 m) exists, above which moulins are unlikely to form (Poinar et al., 2015). More recently, Christoffersen et al. (2018) showed the presence of water-filled crevasses at an elevation of 1800 m in SW Greenland. In this work, our automated method detected, and we visually confirmed, numerous (> 50) rapid lake drainage events above this hypothesized hydrofracture elevation limit, including events at or above 1800 m elevation in both SW and SE Greenland (Fig. 9). While it is not possible to fully confirm the presence of moulins due to the horizontal resolution of the S2 images, these lake drainage events occur between images several (2–3) days apart, with no evidence of overflow drainage, and do not coincide with lake volume decreases for nearby meltwater features. These findings challenge the hypothesis of an upper elevation hydrofracture limit and high-elevation rapid lake drainage events should be investigated in future work.

We further compared lake depth between 2018 and 2019 for different lake types. Previous studies have found little relationship between lake depth and drainage likelihood (Fitzpatrick et al., 2014; Williamson, Willis, et al., 2018). We find that lake depth does appear to control drainage likelihood in some fashion and demonstrate that lake drainage occurrence increases with mean lake depth (Fig. 6). For example, of all 2018 and 2019 supraglacial lakes in SW Greenland with a mean depth > 3 m (45% of all SW GrIS lakes), 41% drain rapidly, a much higher percentage than those that drain rapidly with mean depths < 2 m (8.7%).

Despite expectations that 2019 lakes would be deeper than in 2018, due to it being a warmer melt season, our observations suggest otherwise. Similar to Selmes et al. (2013), we observe cases where 2018 lakes grew larger and deeper than in 2019 when they rapidly drained. Moreover, we find that non-draining lakes were, on average, deeper across all regions during the colder 2018 melt season. We propose three potential explanations for this phenomenon. First, 2019 lake depths may be limited by shallower basins due to the refreezing of meltwater in these basins in 2018. Second, the calculation of lake depth is sensitive to the reflectance of pixels immediately surrounding the lake, a factor that may vary between years.

Third, we suggest that various dynamical controls may initiate rapid lake drainage events at shallower depths during the warmer 2019 melt season. Warmer early melt season air temperatures have substantial hydrological consequences. The earlier melting of surface snow exposes bare ice, crevasses, and fractures, and expedites the development of supraglacial to basal hydrologic routing networks. As such, meltwater can access the bed earlier in a warmer year, enhancing basal slip, a process that has also been shown to initiate rapid lake drainage (Stevens et al., 2015), and thereby increasing localized ice velocity speed-ups earlier in the melt season. Rapid lake drainage events further result in a tensile shock that establishes new surface-to-bed moulins by initiating additional rapid drainage events through a cascading process (Christoffersen et al., 2018). Additionally, elastic stress coupling from one rapid lake drainage event can trigger other nearby lakes to drain (Stevens et al., 2024). We finally hypothesize that lake filling speed may also influence hydrofracture potential, with faster filling lakes at increasing risk of rapid drainage. During the 2019 melt season, these dynamical processes may initiate rapid lake drainages at shallower depths than in 2018, not allowing many lakes to reach their max-

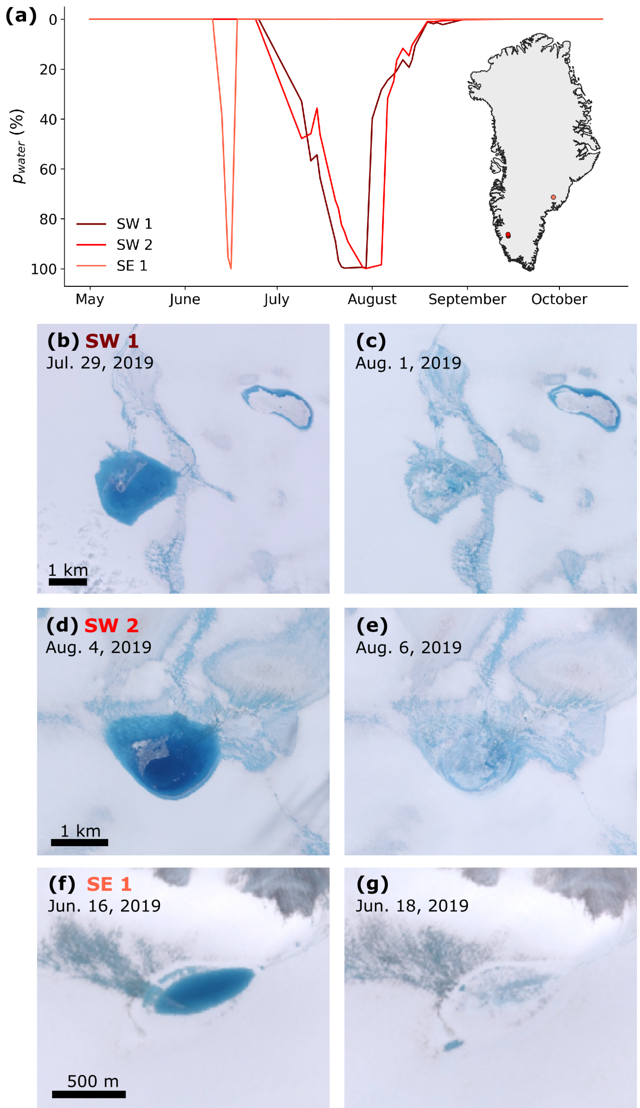

Figure 9. Examples of three high elevation rapid lake drainage events in SW and SE Greenland. (a) Time series of p_{water} for the three lakes, with their locations indicated on the GrIS map. (b,c) Sentinel-2 imagery before (b) and after (c) the rapid drainage of lake SW 1, located at 1898 m elevation. (d,e) Sentinel-2 imagery before (d) and after (e) the rapid drainage of lake SW 2, located at 1887 m elevation. (f,g) Sentinel-2 imagery before (f) and after (g) the rapid drainage of lake SE 1, located at 1793 m elevation.

imum 2018 extent. These potential controls on rapid lake drainage should be further investigated in future work.

Finally, earlier rapid lake drainage events and surface-to-bed moulin development facilitate a prolonged influx of meltwater to the ice-bed interface (Banwell et al., 2016). This accelerated development of the supraglacial, englacial and subglacial hydrological routing systems in warmer melt seasons may explain the substantial increase in 2019 slowly draining lakes. Conversely, in cooler years, the hydrological network may not be fully developed to facilitate efficient meltwater drainage when air temperatures drop in the fall, resulting in a greater proportion of refreezing lakes.

5.1 Limitations and uncertainty

5.1.1 Supraglacial lake types

Distinguishing between rapidly and slowly draining lakes is a non-trivial task, with various definitions proposed in the literature (Das et al., 2008; Williamson, Willis, et al., 2018; Morriss et al., 2013). Here, we follow Morriss et al. (2013) by adopting a more conservative definition (6 days) in constructing our training dataset to accommodate the occasionally limited temporal resolution of clear-sky optical imagery. The implications of this may be the categorization of some lakes as rapidly draining, while other studies would consider them slowly draining. Additionally, drainage events occurring towards the end of the melt season (mid-late August) may be misclassified as refreezing, as both events involve a sharp decrease in water presence. Our testing dataset reveals that differentiating between refreeze and slow drain classifications is the most challenging, with all misclassifications occurring between these two classes (Fig. S4). Some lakes may both partially drain and then refreeze, further complicating this distinction.

The labeled lakes used for model training and testing were lakes where we could clearly distinguish the classification. However, this is not the case for all lakes on which the algorithm was applied. We test the robustness of our findings and quantify uncertainty by comparing our results with those from the subset of lakes where the $ROCKET_{op}$ and $ROCKET_{mic}$ classifications agree, as we believe these cases have the highest certainty. For $\sim$3% of the 9992 total lakes there is either insufficient optical or microwave imagery and thus only one model can be used for the classification. Disregarding buried lake classifications (as the $ROCKET_{op}$ will never be able to classify buried lakes), the two models further disagree for 28% of the lakes' classifications.

The two models disagree most frequently, and thus the uncertainty is highest, in the SW and NE regions (32% disagreement in both regions). The uncertainty is lowest in CW Greenland, with 23% disagreement between the two models (Fig. S5). As slow drainages can be easily confused between both rapid drainage and refreeze, we understandably find the highest disagreement between $ROCKET_{op}$ and $ROCKET_{mic}$ for the slow drainage class (Fig. S5).

For the majority of cases in which the two models disagree (87%), the final classification aligns with that from $ROCKET_{op}$. This makes sense as S1 backscatter can be noisy, particularly for smaller lakes, and depends on factors other than liquid water presence (i.e. volume scattering, surface roughness, satellite geometry). Figure S6 shows changes to the lake type proportions (ignoring buried lakes) when only considering these lakes with higher confidence classifications (where the $ROCKET_{op}$ and $ROCKET_{mic}$ models agree). We find minimal changes in the proportion of lake classifications in the SW and CW regions. In NO and SE Greenland, we see that the proportion of refreezing lakes increases and the proportion of slowly draining lakes decreases when only considering these higher confidence lakes. However, the pattern of interannual changes between 2018 and 2019, described above in the results, remains robust.

5.1.2 Supraglacial lake depths

We retrieved lake depth from optical imagery using a radiative transfer equation (Pope et al., 2016; Williamson, Banwell, et al., 2018), which is known to systematically underestimate lake depths using the red band and overestimate shallow lake depths using the green band (Melling et al., 2024; Lutz et al., 2024). Given the known limitations of this method, we do not recommend using the absolute lake values shown here to prescribe lake depth and volume limits for hydrofracture. We chose to use this radiative transfer method for obtaining lake depths due to its ability to scale to the entire Greenland Ice Sheet easily.

From our lake depth analysis, we highlight two key findings: 1) lake drainage occurrence increases as lake depth increases and 2) non-draining lakes were deeper in 2018 than in 2019, despite 2018 being a colder melt season. Lake depths calculated using various bands in the radiative transfer equation are positively correlated with depths calculated using other bands and from other methods (e.g. ICESat-2, depression topography method, empirical formulation) (Pope et al., 2016; Melling et al., 2024). As such, we expect that these two findings, which focus on a relative lake depth comparison between lake classes and melt seasons, to remain robust.

6 Conclusions

In this work we build upon previous, regional supraglacial lake evolution studies by providing an GrIS-wide data set covering the fate of nearly 10,000 supraglacial lakes during the 2018 and 2019 melt seasons. We first develop a new time series classification method that incorporates optical and microwave imagery to classify GrIS supraglacial lakes into four categories automatically: 1) refreeze, 2) rapid drainage, 3) slow drainage, and 4) buried. We then apply our method to supraglacial lakes detected during the 2018 and 2019 melt seasons, enabling us to compare lake characteristics between the two years, and provide new insights into factors controlling lake evolution and drainage.

We demonstrate that substantial interannual variability in lake evolution exists between the cooler 2018 and warmer 2019 melt seasons, a finding that is robust to uncertainty in our classifications. An increasing proportion of lake drainage events in a warmer year may indicate a non-linearity in the potential for hydrofracture with increasing summer air temperatures. We further provide evidence for several high elevation lake drainage events, above the previously hypothesized 1600 m elevation hydrofracture limit (Poinar et al., 2015). Our results additionally suggest that mean lake depth is related to drainage potential, as the proportion of draining lakes increases with mean depth. However, we surprisingly find deeper non-draining lakes during the cooler 2018 melt season, a topic that should be the focus of future work. The novel supraglacial lake classification method presented here, and the unique resulting dataset, provide important new insight into lake drainage and refreeze and will be useful for future GrIS supraglacial lake and hydrofracture research.

7 Open Research

GrIS supraglacial lake outlines from the 2018 and 2019 melt seasons can be found at: `https://zenodo.org/records/4813833`. All satellite imagery used is freely available on Google Earth Engine (GEE) at the following GEE identifier snippets – Sentinel 1: ee.ImageCollection("COPERNICUS/S1_GRD"), Sentinel 2: ee.ImageCollection("COPERNICUS/S2_HARMONIZED"), and Landsat 8: ee.ImageCollection("LANDSAT/LC08/C02/T1_TOA"). CARRA data is publicly available on Copernicus' C3S Climate Data Store (DOI: DOI: 10.24381/cds.713858f6)

Time series model classification code and output can be obtained by request during the review process and will be made publicly available on Zenodo after review.

8 Author Contributions

DD initially designed the study and led the analysis and writing. ACS and AFB helped interpret the results of the study. EH and MOG contributed to the machine learning model selection, training, and cross-validation. HY helped label supraglacial lakes for model training and helped prepare figures. BM provided and processed CARRA near-surface temperature data. All authors helped with writing and editing the manuscript.

Acknowledgments

DD, ACS, EH, MOG and AFB were supported by the iHARP HDR Institute (NSF award #2118285). We acknowledge high-performance computing support from Cheyenne (`https://doi.org/10.5065/D6RX99HX`) provided by NCAR's Computational and Information Systems Laboratory, sponsored by the NSF. This work also utilized the Summit supercomputer, which is supported by the NSF (awards ACI-1532235 and ACI-1532236) and is a joint effort of the University of Colorado Boulder, and Colorado State University.

References

Banwell, A. F., Arnold, N. S., Willis, I. C., Tedesco, M., & Ahlstrm, A. P. (2012). Modeling supraglacial water routing and lake filling on the Greenland Ice Sheet. *Journal of Geophysical Research: Earth Surface*. doi: 10.1029/2012JF002393

Banwell, A. F., Caballero, M., Arnold, N. S., Glasser, N. F., Cathles, L. M., & MacAyeal, D. R. (2014). Supraglacial lakes on the Larsen B ice shelf, Antarctica, and at Paakitsoq, West Greenland: A comparative study. *Annals of Glaciology*, *55*(66), 1–8. doi: 10.3189/2014AoG66A049

Banwell, A. F., Hewitt, I., Willis, I., & Arnold, N. (2016). Moulin density controls drainage development beneath the Greenland ice sheet. *Journal of Geophysical Research: Earth Surface*, *121*(12), 2248–2269. doi: 10.1002/2015JF003801

Banwell, A. F., Willis, I. C., Macdonald, G. J., Goodsell, B., & MacAyeal, D. R. (2019). Direct measurements of ice-shelf flexure caused by surface meltwater ponding and drainage. *Nature Communications*. doi: 10.1038/s41467-019-08522-5

Bartholomaus, T. C., Anderson, R. S., & Anderson, S. P. (2008). Response of glacier basal motion to transient water storage. *Nature Geoscience*, *1*(1), 33–37. doi: 10.1038/ngeo.2007.52

Bartholomew, I., Nienow, P., Mair, D., Hubbard, A., King, M. A., & Sole, A. (2010, 6). Seasonal evolution of subglacial drainage and acceleration in a Greenland outlet glacier. *Nature Geoscience*, *3*(6), 408–411. doi: 10.1038/ngeo863

Benedek, C. L., & Willis, I. C. (2021). Winter drainage of surface lakes on the Greenland Ice Sheet from Sentinel-1 SAR imagery. *The Cryosphere*, *15*(3), 1587–1606. Retrieved from `https://tc.copernicus.org/articles/15/1587/2021/` doi: 10.5194/tc-15-1587-2021

Box, J. E., & Ski, K. (2007). Remote sounding of Greenland supraglacial melt lakes: Implications for subglacial hydraulics. *Journal of Glaciology*, *53*(181), 257–265. doi: 10.3189/172756507782202883

Cabello, N., Naghizade, E., Qi, J., & Kulik, L. (2020). Fast and accurate time series classification through supervised interval search. In *2020 ieee international conference on data mining (icdm)* (pp. 948–953). IEEE.

Catania, G. A., & Neumann, T. A. (2010). Persistent englacial drainage features in the Greenland Ice Sheet. *Geophysical Research Letters*, *37*(2), 1–5. doi: 10

.1029/2009GL041108
Catania, G. A., Neumann, T. A., & Price, S. F. (2008). Characterizing englacial drainage in the ablation zone of the Greenland ice sheet. *Journal of Glaciology*, *54*(187), 567–578. doi: 10.3189/002214308786570854
Christoffersen, P., Bougamont, M., Hubbard, A., Doyle, S. H., Grigsby, S., & Pettersson, R. (2018). Cascading lake drainage on the Greenland Ice Sheet triggered by tensile shock and fracture. *Nature Communications*, *9*(1), 1064. doi: 10.1038/s41467-018-03420-8
Chu, V. W. (2014). Greenland ice sheet hydrology. *Progress in Physical Geography: Earth and Environment*, *38*(1), 19–54. doi: 10.1177/0309133313507075
Daneshgar, A. S., Chu, V. W., Noshad, M., & Yang, K. (2019). Extracting Supraglacial Streams on Greenland Ice Sheet Using High-Resolution Satellite Imagery. In *American geophysical union.* San Francisco. doi: 2019AGUFM.H21N1947D
Das, S. B., Joughin, I., Behn, M. D., Howat, I. M., King, M. A., Lizarralde, D., & Bhatia, M. P. (2008). Fracture Propagation to the Base of the Greenland Ice Sheet During Supraglacial Lake Drainage. *Science*, *320*(5877), 778–781. Retrieved from `https://www.sciencemag.org/lookup/doi/10.1126/science.1153360` doi: 10.1126/science.1153360
Dau, H. A., Keogh, E., Kamgar, K., Yeh, C.-C. M., Zhu, Y., Gharghabi, S., ... Hexagon-ML (2018). *The UCR Time Series Classification Archive.*
Dell, R., Arnold, N., Willis, I., Banwell, A. F., Williamson, A. G., Pritchard, H., & Orr, A. (2020). Lateral meltwater transfer across an Antarctic ice shelf. *The Cryosphere*, *14*(7), 2313–2330. doi: 10.5194/tc-14-2313-2020
Dempster, A., Petitjean, F., & Webb, G. I. (2020). ROCKET: exceptionally fast and accurate time series classification using random convolutional kernels. *Data Mining and Knowledge Discovery*, *34*(5), 1454–1495. doi: 10.1007/s10618-020-00701-z
Deng, H., Runger, G., Tuv, E., & Vladimir, M. (2013). A time series forest for classification and feature extraction. *Information Sciences*, *239*, 142–153. doi: 10.1016/j.ins.2013.02.030
Doyle, S. H., Hubbard, A., Fitzpatrick, A. A. W., van As, D., Mikkelsen, A. B., Pettersson, R., & Hubbard, B. (2014). Persistent flow acceleration within the interior of the Greenland ice sheet. *Geophysical Research Letters*, *41*(3), 899–905. doi: 10.1002/2013GL058933
Dunmire, D., Banwell, A. F., Lenaerts, J., & Datta, R. T. (2021). Contrasting regional variability of buried meltwater extent over two years across the Greenland Ice Sheet. *The Cryosphere Discussions*. doi: 10.5194/tc-2021-3
Echelmeyer, K., Clarke, T. S., & Harrison, W. D. (1991). Surficial glaciology of Jakobshavns Isbrae, West Greenland: part I. Surface morphology. *Journal of Glaciology*, *37*(127), 368–382. doi: 10.1017/S0022143000005803
Fitzpatrick, A. A. W., Hubbard, A. L., Box, J. E., Quincey, D. J., van As, D., Mikkelsen, A. P. B., ... Jones, G. A. (2014). A decade (2002–2012) of supraglacial lake volume estimates across Russell Glacier, West Greenland. *The Cryosphere*, *8*(1), 107–121. doi: 10.5194/tc-8-107-2014
Forster, R. R., Box, J. E., Van Den Broeke, M. R., Miège, C., Burgess, E. W., Van Angelen, J. H., ... McConnell, J. R. (2014). Extensive liquid meltwater storage in firn within the Greenland ice sheet. *Nature Geoscience*. doi: 10.1038/ngeo2043
Glen, E., Leeson, A. A., Banwell, A. F., Maddalena, J., Corr, D., Noël, B., & McMillan, M. (2024). A comparison of supraglacial meltwater features throughout contrasting melt seasons: Southwest Greenland. *The Cryosphere Discussions*.
Gorelick, N., Hancher, M., Dixon, M., Ilyushchenko, S., Thau, D., & Moore, R. (2017). Remote Sensing of Environment Google Earth Engine : Planetary-scale geospatial analysis for everyone. *Remote Sensing of Environment*. doi:

10.1016/j.rse.2017.06.031

Hanna, E., Huybrechts, P., Steffen, K., Cappelen, J., Huff, R., Shuman, C., … Griffiths, M. (2008). Increased Runoff from Melt from the Greenland Ice Sheet: A Response to Global Warming. *Journal of Climate*, *21*(2), 331–341. doi: 10.1175/2007JCLI1964.1

Harper, J., Humphrey, N., Pfeffer, W. T., Brown, J., & Fettweis, X. (2012). Greenland ice-sheet contribution to sea-level rise buffered by meltwater storage in firn. *Nature*. doi: 10.1038/nature11566

Hochreuther, P., Neckel, N., Reimann, N., Humbert, A., & Braun, M. (2021). Fully automated detection of supraglacial lake area for northeast greenland using sentinel-2 time-series. *Remote Sensing*, *13*(2), 1–24. doi: 10.3390/rs13020205

Hoffman, M. J., Catania, G. A., Neumann, T. A., Andrews, L. C., & Rumrill, J. A. (2011). Links between acceleration, melting, and supraglacial lake drainage of the western Greenland Ice Sheet. *Journal of Geophysical Research: Earth Surface*, *116*(4), 1–16. doi: 10.1029/2010JF001934

Howat, I. M., de la Peña, S., van Angelen, J. H., Lenaerts, J. T. M., & van den Broeke, M. R. (2013). <i>Brief Communication</i> "Expansion of meltwater lakes on the Greenland Ice Sheet". *The Cryosphere*. doi: 10.5194/tc-7-201-2013

Howat, I. M., Negrete, A., & Smith, B. E. (2015). MEaSUREs Greenland Ice Sheet Mapping Project (GIMP) Digital Elevation Model. *Boulder: NASA National Snow and Ice Data Center Distributed Active Archive Center*.

Johansson, A. M., & Brown, I. A. (2013). Adaptive Classification of Supra-Glacial Lakes on the West Greenland Ice Sheet. *IEEE Journal of Selected Topics in Applied Earth Observations and Remote Sensing*, *6*(4), 1998–2007. doi: 10.1109/JSTARS.2012.2233722

Johansson, A. M., Jansson, P., & Brown, I. A. (2013). Spatial and temporal variations in lakes on the Greenland Ice Sheet. *Journal of Hydrology*. doi: 10.1016/j.jhydrol.2012.10.045

Jullien, N., Tedstone, A. J., Machguth, H., Karlsson, N. B., & Helm, V. (2023). Greenland Ice Sheet Ice Slab Expansion and Thickening. *Geophysical Research Letters*, *50*(10). doi: 10.1029/2022GL100911

Karim, F., Majumdar, S., Darabi, H., & Harford, S. (2019). Multivariate LSTM-FCNs for time series classification. *Neural Networks*, *116*, 237–245. doi: 10.1016/j.neunet.2019.04.014

Koenig, L. S., Lampkin, D. J., Montgomery, L. N., Hamilton, S. L., Turrin, J. B., Joseph, C. A., … Gogineni, P. (2015). Wintertime storage of water in buried supraglacial lakes across the Greenland Ice Sheet. *Cryosphere*. doi: 10.5194/tc-9-1333-2015

Law, R., Arnold, N., Benedek, C., Tedesco, M., Banwell, A. F., & Willis, I. (2020). Over-winter persistence of supraglacial lakes on the Greenland Ice Sheet: Results and insights from a new model. *Journal of Glaciology*. doi: 10.1017/jog.2020.7

Leeson, A. A., Shepherd, A., Briggs, K., Howat, I., Fettweis, X., Morlighem, M., & Rignot, E. (2015). Supraglacial lakes on the Greenland ice sheet advance inland under warming climate. *Nature Climate Change*. doi: 10.1038/nclimate2463

Löning, M., Bagnall, A., Ganesh, S., Kazakov, V., Lines, J., & Király, F. J. (2019). sktime: A Unified Interface for Machine Learning with Time Series. *ArXiV*.

Lutz, K., Sommer, C., Humbert, A., & Braun, M. (2024). Evaluation of supraglacial lake depth estimation techniques using Sentinel-2, ICESat-2, TanDEM-X, and in situ data, along with an analysis of rapid drainage events over Northeast Greenland. In *Egu general assembly 2024.* Vienna, Austria.

Macdonald, G. J., Banwell, A. F., & MacAyeal, D. R. (2018). Seasonal evolution of supraglacial lakes on a floating ice tongue, Petermann Glacier, Greenland. *An-*

nals of Glaciology, *59*(76pt1), 56–65. doi: 10.1017/aog.2018.9

MacFerrin, M., Machguth, H., As, D. v., Charalampidis, C., Stevens, C. M., Heilig, A., … Abdalati, W. (2019). Rapid expansion of Greenland's low-permeability ice slabs. *Nature*, *573*(7774), 403–407. Retrieved from https://doi.org/10.1038/s41586-019-1550-3 doi: 10.1038/s41586-019-1550-3

Machguth, H., Macferrin, M., Van As, D., Box, J. E., Charalampidis, C., Colgan, W., … Van De Wal, R. S. (2016). Greenland meltwater storage in firn limited by near-surface ice formation. *Nature Climate Change*. doi: 10.1038/nclimate2899

McMillan, M., Nienow, P., Shepherd, A., Benham, T., & Sole, A. (2007). Seasonal evolution of supra-glacial lakes on the Greenland Ice Sheet. *Earth and Planetary Science Letters*. doi: 10.1016/j.epsl.2007.08.002

Melling, L., Leeson, A., McMillan, M., Maddalena, J., Bowling, J., Glen, E., … Lørup Arildsen, R. (2024). Evaluation of satellite methods for estimating supraglacial lake depth in southwest Greenland. *The Cryosphere*, *18*(2), 543–558. doi: 10.5194/tc-18-543-2024

Middlehurst, M., Large, J., & Bagnall, A. (2020). The Canonical Interval Forest (CIF) Classifier for Time Series Classification. In *2020 ieee international conference on big data* (pp. 188–195). IEEE.

Mikkelsen, A. B., Hubbard, A., Macferrin, M., Eric Box, J., Doyle, S. H., Fitzpatrick, A., … Pettersson, R. (2016). Extraordinary runoff from the Greenland ice sheet in 2012 amplified by hypsometry and depleted firn retention. *Cryosphere*, *10*(3), 1147–1159. doi: 10.5194/tc-10-1147-2016

Miles, K. E., Willis, I. C., Benedek, C. L., Williamson, A. G., & Tedesco, M. (2017). Toward monitoring surface and subsurface lakes on the Greenland ice sheet using sentinel-1 SAR and landsat-8 OLI imagery. *Frontiers in Earth Science*, *5*(July), 1–17. doi: 10.3389/feart.2017.00058

Moez, A. (2020). *PyCaret: An open source, low-code machine learning library in Python.*

Morriss, B. F., Hawley, R. L., Chipman, J. W., Andrews, L. C., Catania, G. A., Hoffman, M. J., … Neumann, T. A. (2013). A ten-year record of supraglacial lake evolution and rapid drainage in West Greenland using an automated processing algorithm for multispectral imagery. *Cryosphere*, *7*(6), 1869–1877. doi: 10.5194/tc-7-1869-2013

Moussavi, M. S., Abdalati, W., Pope, A., Scambos, T., Tedesco, M., MacFerrin, M., & Grigsby, S. (2016). Derivation and validation of supraglacial lake volumes on the Greenland Ice Sheet from high-resolution satellite imagery. *Remote Sensing of Environment*, *183*, 294–303. Retrieved from http://dx.doi.org/10.1016/j.rse.2016.05.024 doi: 10.1016/j.rse.2016.05.024

Moussavi, M. S., Pope, A., Halberstadt, A. R. W., Trusel, L. D., Cioffi, L., & Abdalati, W. (2020). Antarctic Supraglacial Lake Detection Using Landsat 8 and Sentinel-2 Imagery: Towards Continental Generation of Lake Volumes. *remote sensing*, *12*(1).

Otto, J., Holmes, F. A., & Kirchner, N. (2022). Supraglacial lake expansion, intensified lake drainage frequency, and first observation of coupled lake drainage, during 1985–2020 at Ryder Glacier, Northern Greenland. *Frontiers in Earth Science*, *10*. doi: 10.3389/feart.2022.978137

Pedregosa, F., Varoquaux, G., Gramfort, A., Michel, V., Thirion, B., Grisel, O., … Duchesnay, E. (2011). Scikit-learn: Machine Learning in Python. *Journal of Machine Learning Research*, *12*, 2825–2830.

Poinar, K., Joughin, I., Das, S. B., Behn, M. D., Lenaerts, J. T. M., & Broeke, M. R. (2015). Limits to future expansion of surface-melt-enhanced ice flow into the interior of western Greenland. *Geophysical Research Letters*, *42*(6), 1800–1807. Retrieved from https://onlinelibrary.wiley.com/doi/abs/10.1002/2015GL063192 doi: 10.1002/2015GL063192

Pope, A., Scambos, T. A., Moussavi, M., Tedesco, M., Willis, M., Shean, D., & Grigsby, S. (2016). Estimating supraglacial lake depth in West Greenland using Landsat 8 and comparison with other multispectral methods. *Cryosphere*, *10*(1), 15–27. doi: 10.5194/tc-10-15-2016

Prokhorenkova, L., Gusev, G., Vorobev, A., Dorogush, A. V., & Gulin, A. (2018). CatBoost: Unbiased Boosting with Categorical Features. In *Proceedings of the 32nd international conference on neural information processing systems* (pp. 6639–6649). Red Hook, NY, USA: Curran Associates Inc.

Rignot, E., Echelmeyer, K., & Krabill, W. (2001). Penetration depth of interferometric synthetic-aperture radar signals in snow and ice. *Geophysical Research Letters*. doi: 10.1029/2000GL012484

Rignot, E., & Mouginot, J. (2012). Ice flow in Greenland for the International Polar Year 2008-2009. *Geophysical Research Letters*. doi: 10.1029/2012GL051634

Schröder, L., Neckel, N., Zindler, R., & Humbert, A. (2020). Perennial Supraglacial Lakes in Northeast Greenland Observed by Polarimetric SAR. *Remote Sensing*, *12*(17), 2798. Retrieved from `https://www.mdpi.com/2072-4292/12/17/2798` doi: 10.3390/rs12172798

Schyberg, H., Yang, X., Køltzow, M., Amstrup, B., Bakketun, , Bazile, E., ... Wang, Z. (2020). *Arctic regional reanalysis on single levels from 1991 to present.*

Selmes, N., Murray, T., & James, T. D. (2011). Fast draining lakes on the Greenland Ice Sheet. *Geophysical Research Letters*. doi: 10.1029/2011GL047872

Selmes, N., Murray, T., & James, T. D. (2013). Characterizing supraglacial lake drainage and freezing on the Greenland Ice Sheet. *The Cryosphere Discussions*.

Stevens, L. A., Behn, M. D., McGuire, J. J., Das, S. B., Joughin, I., Herring, T., ... King, M. A. (2015). Greenland supraglacial lake drainages triggered by hydrologically induced basal slip. *Nature*, *522*(7554), 73–76. doi: 10.1038/nature14480

Stevens, L. A., Das, S. B., Behn, M. D., McGuire, J. J., Lai, C., Joughin, I., ... Nettles, M. (2024). Elastic Stress Coupling Between Supraglacial Lakes. *Journal of Geophysical Research: Earth Surface*, *129*(5). doi: 10.1029/2023JF007481

Sundal, A. V., Shepherd, A., Nienow, P., Hanna, E., Palmer, S., & Huybrechts, P. (2009). Evolution of supra-glacial lakes across the Greenland Ice Sheet. *Remote Sensing of Environment*, *113*(10), 2164–2171. Retrieved from `http://dx.doi.org/10.1016/j.rse.2009.05.018` doi: 10.1016/j.rse.2009.05.018

Tedesco, M., Willis, I. C., Hoffman, M. J., Banwell, A. F., Alexander, P., & Arnold, N. S. (2013). Ice dynamic response to two modes of surface lake drainage on the Greenland ice sheet. *Environmental Research Letters*. doi: 10.1088/1748-9326/8/3/034007

Tedstone, A. J., & Machguth, H. (2022). Increasing surface runoff from Greenland's firn areas. *Nature Climate Change*, *12*(7), 672–676. doi: 10.1038/s41558-022-01371-z

Trusel, L. D., Das, S. B., Osman, M. B., Evans, M. J., Smith, B. E., Fettweis, X., ... van den Broeke, M. R. (2018). Nonlinear rise in Greenland runoff in response to post-industrial Arctic warming. *Nature*, *564*(7734), 104–108. doi: 10.1038/s41586-018-0752-4

Trusel, L. D., Frey, K. E., Das, S. B., Karnauskas, K. B., Kuipers Munneke, P., Van Meijgaard, E., & Van Den Broeke, M. R. (2015). *Divergent trajectories of Antarctic surface melt under two twenty-first-century climate scenarios.* doi: 10.1038/ngeo2563

Turton, J. V., Hochreuther, P., Reimann, N., & Blau, M. T. (2021, 8). The distribution and evolution of supraglacial lakes on 79° N Glacier (north-eastern Greenland) and interannual climatic controls. *The Cryosphere*, *15*, 3877–3896. doi: 10.5194/tc-15-3877-2021

Wang, Y., & Sugiyama, S. (2024, 3). Supraglacial lake evolution on Tracy and Heilprin Glaciers in northwestern Greenland from 2014 to 2021. *Remote Sensing of Environment*, *303*, 114006. doi: 10.1016/j.rse.2024.114006

Williamson, A. G., Arnold, N. S., Banwell, A. F., & Willis, I. C. (2017). A Fully Automated Supraglacial lake area and volume Tracking ("FAST") algorithm: Development and application using MODIS imagery of West Greenland. *Remote Sensing of Environment*. doi: 10.1016/j.rse.2017.04.032

Williamson, A. G., Banwell, A. F., Willis, I. C., & Arnold, N. S. (2018). Dual-satellite (Sentinel-2 and Landsat 8) remote sensing of supraglacial lakes in Greenland. *The Cryosphere*, *12*(9), 3045–3065. Retrieved from `https://tc.copernicus.org/articles/12/3045/2018/` doi: 10.5194/tc-12-3045-2018

Williamson, A. G., Willis, I. C., Arnold, N. S., & Banwell, A. F. (2018). Controls on rapid supraglacial lake drainage in West Greenland: An Exploratory Data Analysis approach. *Journal of Glaciology*. doi: 10.1017/jog.2018.8

Yang, K., & Smith, L. C. (2013). Supraglacial streams on the greenland ice sheet delineated from combined spectral-shape information in high-resolution satellite imagery. *IEEE Geoscience and Remote Sensing Letters*, *10*(4), 801–805. doi: 10.1109/LGRS.2012.2224316

Zhang, W., Yang, K., Smith, L. C., Wang, Y., van As, D., Noël, B., ... Liu, J. (2023, 11). Pan-Greenland mapping of supraglacial rivers, lakes, and water-filled crevasses in a cool summer (2018) and a warm summer (2019). *Remote Sensing of Environment*, *297*, 113781. doi: 10.1016/j.rse.2023.113781

Zheng, L., Li, L., Chen, Z., He, Y., Mo, L., Chen, D., ... Cheng, X. (2023). Multi-sensor imaging of winter buried lakes in the Greenland Ice Sheet. *Remote Sensing of Environment*, *295*, 113688. doi: 10.1016/j.rse.2023.113688

Zwally, H. J., Abdalati, W., Herring, T., Larson, K., Saba, J., & Steffen, K. (2002). Surface Melt – Induced Acceleration of Greenland Ice-Sheet Flow. *Science*, *297*(July), 218–223.